Cement and Concrete Research 39 (2009) 529–536

Contents lists available at ScienceDirect

Cement and Concrete Research

journal homepage: http://ees.elsevier.com/CEMCON/default.asp

Investigating the thermo-mechanical behaviour of cementitious materials using image processing techniques

V. Huon *, B. Cousin, B. Wattrisse, O. Maisonneuve

Laboratoire de Mécanique et Génie Civil, Université Montpellier 2, Place Eugène Bataillon, 34095 Montpellier cedex 5, France

ARTICLE INFO

Article history:
Received 12 June 2007
Accepted 3 March 2009

Keywords:
Infrared thermography
Image analysis
Mechanical properties
Concrete
High-performance concrete

ABSTRACT

Infrared thermography and Digital Image Correlation were used to analyse the mechanical behaviour of mortar, concrete, and high-performance concrete specimens under quasi-static loads. For specimens under compressive loads, Infrared thermography clearly showed the thermo-elastic coupling as well as thermal dissipations due to the microcracking state of freeze/thaw damaged concrete specimens. During an up to failure compressive test, localized thermal effects were observed at the macro-crack location before it appeared. Strain fields at the surface of steel-fibre high-performance concrete specimens under tensile and flexural loadings were determined using the Digital Image Correlation (DIC) technique. These experiments showed that the strain fields early became inhomogeneous. Strains concentrated in multiple localization zones which highlighted the role of the steel fibres in transmitting the internal forces.

1. Introduction

During the last few decades, image processing methods have been successfully used for the thermo-mechanical analysis of the behaviour of materials. Infrared thermography permits the surface temperature field to be measured and its evolution to be recorded in relation to the mechanical load. Hence, thermal dissipations can be quantified resulting in more accurate behavioural models [1,2]. The Digital Image Correlation technique (DIC), allows the surface strain field to be accurately determined. In particular, localization effects, which cannot be highlighted by classical extensometric techniques, can be clearly quantified [3–10].

Despite their high efficiency, image processing methods have seldom been applied to concrete. One of the first applications of DIC to concrete is due to Choi and Shah in 1997 [5], who highlighted highly non-uniform deformations in concrete specimens under compression even in the elastic range. In 2001, Lawler et al. [11] studied three dimensional damage of concrete under compression and used DIC to determine crack patterns. Recently, Corr et al. [12] used DIC to study the bond between carbon-fibre reinforced polymers (CFRP) and concrete substrates as well as the damage of the interfacial transition zone between the aggregates and the surrounding mortar.

Thermal imaging techniques are generally not considered for the study of cement based materials due to the expected weakness of the thermal effects related to concrete deformation. An exception occurred for dynamic loads [1].

However, the performance of cementitious materials is increasing allowing, for example, more slender structures to be designed. Improved behaviour models of high-performance concrete require new experimental tools allowing more accurate investigations to be performed.

This paper aims to present some applications of image processing techniques successfully applied to the study of the behaviour of cementitious materials. Infrared thermography as well as Digital Image Correlation (DIC) were used for various concrete specimens under various loadings. Some effects related to strains, damage and failure are reported either for ordinary concrete or steel-fibre high-performance concrete (SFHPC), i.e. a Reactive Powder Concrete [13,14].

Experimental setups are described in the next section. Section 3 presents thermal effects observed under quasi-static and cyclic compressive loads, while Section 4 deals with strain fields recorded during tensile and bending tests.

2. Experimental setups

2.1. Infrared thermal imaging

The experimental setup consists of a testing machine DARTEC ± 100 kN or MFL UED40 400 kN associated with an infrared camera AGEMA 880 sw or CEDIP JADE 3 mw. The thermal performance of an infrared camera is characterized by the "Noise Equivalent Temperature Distorsion" (NETD) that is the temperature variation equivalent to the effective value of the thermal signal noise. The NETD was 0.2 °C at 30 °C for the AGEMA camera and 0.025 °C at 35 °C for the CEDIP camera for an integration time of 1.5 ms. The camera is connected to a control and acquisition chain including a digitization and storage

* Corresponding author. Tel.: +33 4 67 14 47 37; fax: +33 4 67 14 47 92.
E-mail address: huon@lmgc.univ-montp2.fr (V. Huon).

0008-8846/$ – see front matter © 2009 Elsevier Ltd. All rights reserved.
doi:10.1016/j.cemconres.2009.03.008

Table 1
Composition of the study materials.

Standard mortar			
Cement CEMII/B 32.5R		450 kg m^{-3}	
Standard sand 0/2 mm		1350 kg m^{-3}	C/S = 0.3
Water		225 kg m^{-3}	W/C = 0.5
Steel-fibre high-performance concrete (RPC200)			
High performance cement		950 kg m^{-3}	
Silica fume		225 kg m^{-3}	
Quartz sand 150–600 μm		382 kg m^{-3}	C/S = 0.4
Superplasticizer polyacrylate		17 kg m^{-3}	1.8% C
Water		180 kg m^{-3}	W/C = 0.19
Steel fibres $\emptyset$ = 0.15 mm, L = 13 mm		146 and 235 kg m^{-3}	2 and 3 %vol.
Plain concrete damaged by freezing–thawing cycles			
Cement CEM I 42.5 R		530 kg m^{-3}	
Siliceous sand	0.5–1.6 mm	727 kg m^{-3}	C/S = 0.36
	1–3.2 mm	291 kg m^{-3}	
	2–4 mm	436 kg m^{-3}	
Water		265 kg m^{-3}	W/C = 0.5

assembly and a processing micro-computer. The camera acquires 256 × 320 pixels images of the observed face of the specimen. The maximum acquisition rate is 6.25 thermo-images per second for the AGEMA camera and 40 thermo-images per second for the CEDIP camera. The observed face of the specimen, 40 to 150 mm width and 80 to 300 mm height, is coated with a flat black paint in order to maximize its emissivity. Details about principles of infrared thermography can be found in [2]. Surface temperature maps are obtained after calibrating and filtering the thermo-signal.

2.2. Digital Image Correlation

For the Digital Image Correlation technique, a CCD matrix digital camera PANASONIC WV-CP410 is used in association with the testing machines previously mentioned. The camera acquires 570 × 780 pixels images of the observed face of the specimen. The acquisition rate is 2 images per second. A material point is tracked between two successive images owing to the light intensity distribution in its neighborhood. To this end, a speckle pattern is created on the observed face by spraying white paint. This allows the displacement field to be determined during the test. Kinematic parameters such as strain, strain rate, speed, and acceleration result from computation of derivatives of the displacement field locally approximated by a polynomial function using a least square fitting. The method has been implemented in an image processing software developed in our laboratory. More details about the DIC algorithm used, the derivation method and their implementation are given in [7,8].

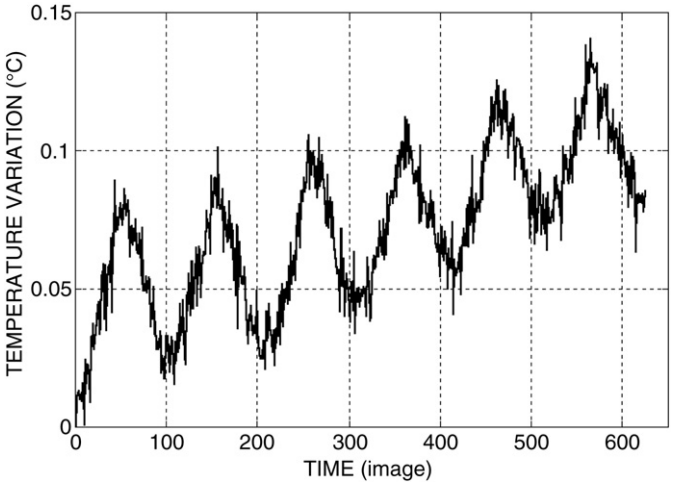

Fig. 2. Time variation of the temperature at midpoint of the mortar specimen under cyclic quasi-static compressive load.

3. Thermal effects of a compressive load on a concrete specimen

3.1. Compressive quasi-static cyclic tests on undamaged mortar and steel-fibre high-performance concrete

Mortar specimens were subjected to compressive quasi-static cyclic loads. The composition of the mortar is given in Table 1. The dimensions of the test specimens were 40 × 40 × 80 mm^3. Six loading cycles were applied between the limits 0–40 MPa. The controlled test parameter was the crosshead speed fixed at 0.05 mm s^{-1}. The temperature map of the observed face of a specimen was monitored and filtered. The thermal chart shown in Fig. 1 represents the variation of the temperature profile along the lengthwise axis of the sample versus the image number, i.e. time. On this chart, the superimposed curve represents the time variation of the compressive stress.

Fig. 2 represents the time variation of the temperature at the midpoint of the test specimen.

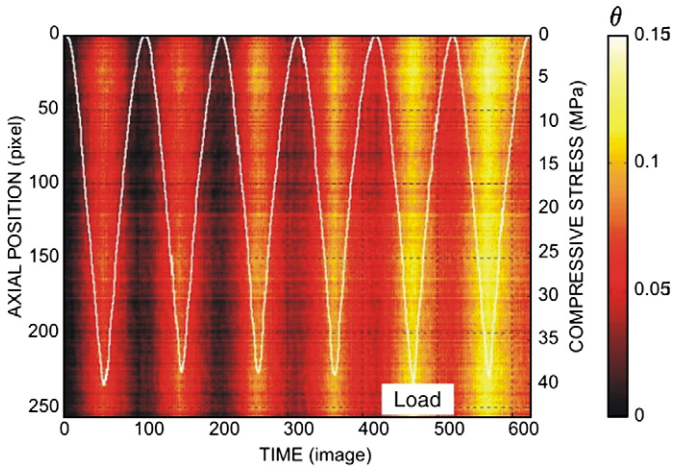

Fig. 1. Applied stress and time variation of the temperature deviation along the lengthwise axis of a mortar specimen under cyclic quasi-static compressive loading (acquisition rate: 5 images/second). Vertically 250 pixels correspond to 60 mm.

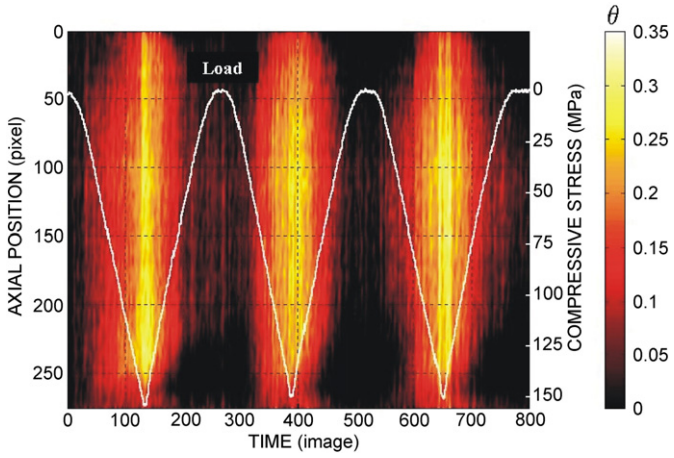

Fig. 3. Applied stress and time variation of the temperature deviation profile along the lengthwise axis of a SFHPC specimen under cyclic quasi-static compressive loading (acquisition rate: 6.25 images/second). Vertically 250 pixels correspond to 140 mm.

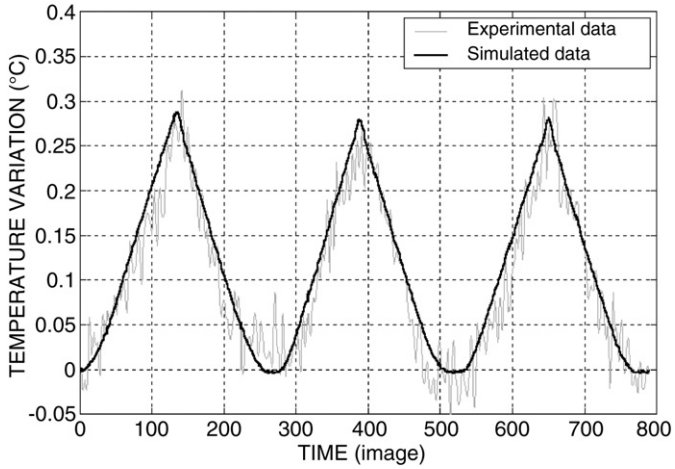

Fig. 4. Time variation of the temperature at midpoint of the SFHPC specimen under cyclic quasi-static compressive load. Comparison between theoretical thermo-elastic coupling and experimental data.

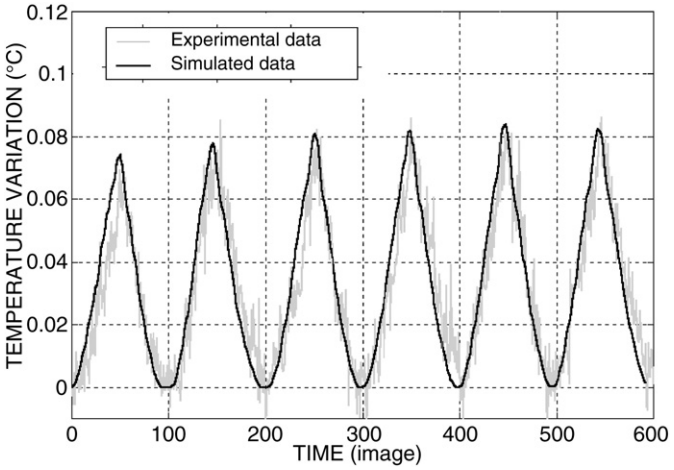

Fig. 5. Comparison between theoretical thermo-elastic coupling and drift-corrected experimental data for mortar specimen.

Figs. 1 and 2 highlight two phenomena:

- Variations of temperature in phase with the variations of the load with an amplitude of 0.08 °C,
- A slight over-all increase of the mean temperature of the test specimen raising 0.04 °C over the experiment duration.

The first effect can be attributed to thermo-elastic coupling [15] which is associated with reversible variations of heat sources related to the variations of the applied load: positive heat sources in compression and negative heat sources in tension. These heat sources generate a temperature increase in compression and a temperature decrease in tension. The relation between heat sources and temperature variations is given by the heat equation which accounts for heat looses by conduction, convection and radiation. In contrast, the actual origin of the second observed thermal effect is not clearly determined. It may be due to:

- A drift of the thermal setup and environment,
- Heat sources due to microscopic phenomena in the concrete. Indeed the maximum applied stress (35 MPa) is close to the compressive strength of the specimen which average value is 45 MPa. Microcracking is likely to occur resulting in dissipative phenomena like friction between the edges of the micro-cracks.

To minimize the relative level of a potential thermal drift, the same experiments were performed with steel-fibre high-performance concrete, which allowed higher stress levels.

Specimens were subjected to three compressive quasi-static cyclic loads between the limits 0 and 150 MPa. The composition of the SFHPC is given in Table 1. The dimensions of the test specimens were $40\times40\times160$ mm^3. The controlled crosshead speed was still fixed at 0.05 mm s^{-1}. The thermal chart is given on Fig. 3, and the time variation of the temperature at the midpoint of the test specimen is represented in Fig. 4. These figures clearly show the thermo-elastic coupling with variations of temperature in phase with the loading cycles. The amplitude of the temperature variations is 0.3 °C. The thermal drift appears to be negligible.

Table 2
Values of physical parameters for thermo-elastic simulations on SFHPC [16,17].

Isotropic dilatation coefficient α	12 10^{-6} K^{-1}
Mass density ρ	2.5 10^3 kg m^{-3}
Specific heat capacity C	840 J kg^{-1} K^{-1}

3.2. Simulation of thermo-elastic coupling and comparison with experiments

As presented in the last section, variations of the temperature in phase with the loading cycles are assumed to be due to the thermo-elastic coupling. To strengthen this assumption, a simple calculation of the thermo-elastic effect can be performed. The first and second principles of thermodynamics lead to the heat diffusion equation. The following linearized form can be considered in the case of the hypotheses given below:

$$\rho C\frac{\partial T}{\partial t} = -T\cdot E\cdot\alpha\cdot\dot{\varepsilon} \tag{1}$$

ρ is the mass density, C the specific heat capacity, T the current temperature, E the elastic modulus, α the isotropic dilatation coefficient and $\dot{\varepsilon}$ the strain rate. In Eq. (1), only the heat source term related to the thermo-elastic coupling has been considered.

Eq. (1) is obtained assuming the following:

- heat sources are spatially homogeneous,
- temperature variations are small,
- local adiabatic conditions are assumed,
- small perturbation hypothesis is considered,
- material is assumed to be homogeneous and isotropic with a linear thermo-elastic behaviour.

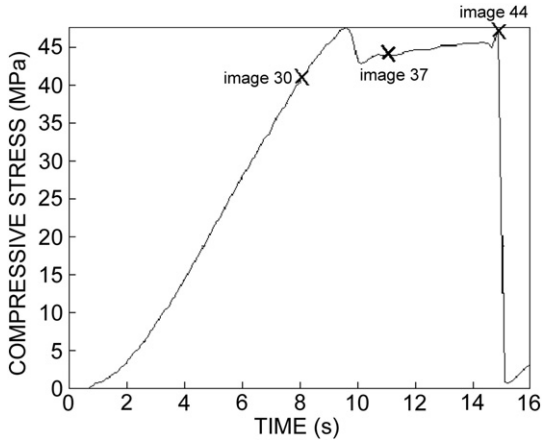

Fig. 6. Time variation of the stress during an up to failure compressive test performed on a mortar specimen.

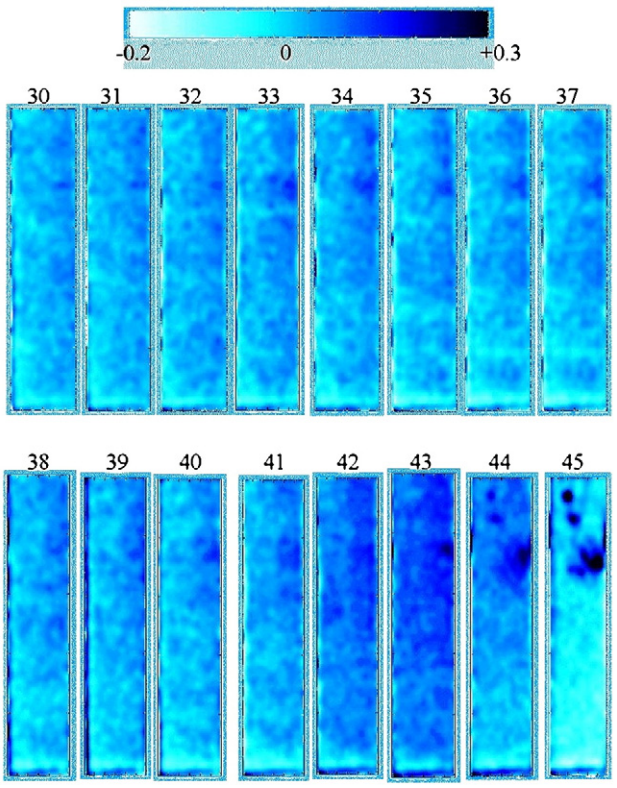

Fig. 7. Thermal images recorded during an up to failure test performed on a mortar specimen (acquisition rate: 2 images per second).

Integrating Eq. (1) leads to the following expression:

$$T - T_0 = \frac{T_0 \alpha \sigma}{\rho C} \tag{2}$$

where σ is the stress.

Values for α, ρ and C, found in the literature [16,17], are given in Table 2.

Fig. 4 shows that the calculated temperatures perfectly match with those measured.

The same simulation was performed for mortar samples to verify if the temperature oscillations shown on Fig. 2 are also due to thermo-elastic effect. To compare the simulation and experiment, the drift observed in Fig. 2 was assumed linear and subtracted from the measured temperature. The comparison between the corrected experimental temperature and the simulated temperature is given in Fig. 5. This figure also shows an excellent agreement between the two curves.

Infrared thermography appears to be an effective technique for analysing the behaviour of concrete under mechanical loads despite the small amplitude of the temperature variations due to thermo-elastic coupling. We show in the following section that IR thermal imaging also makes it possible to observe thermal effects due to damage and cracking phenomena.

3.3. Thermal effects of damage and cracking

Macroscopic effects of damage mainly consist in a decrease of stiffness and strength of the material. From a microscopic point of view, it corresponds to the apparition of micro-cracks, which become more and more numerous and connected. When the material deforms, friction

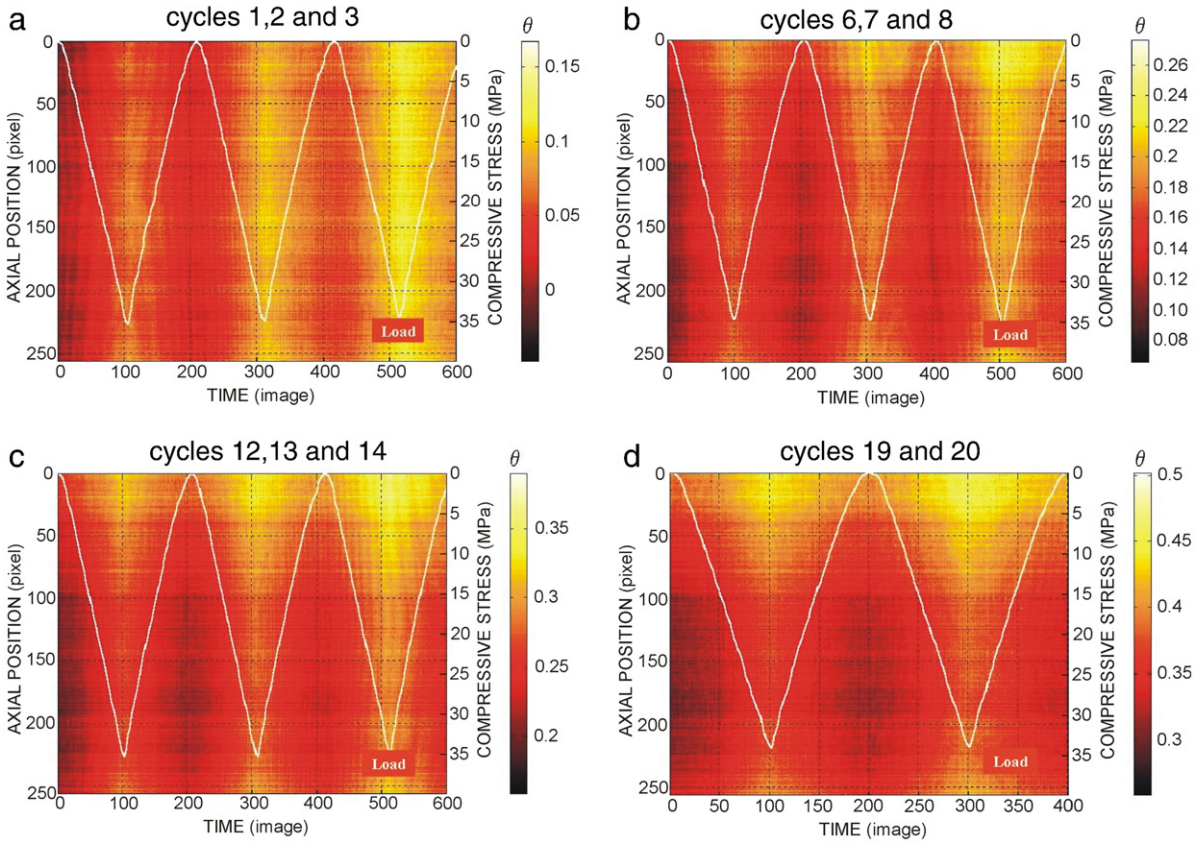

Fig. 8. Applied stress and time variation of the temperature deviation profile along the lengthwise axis of a specimen (marked 1563F6) damaged by freezing–thawing cycles subjected to cyclic quasi-static compressive loading (acquisition rate: 5 images/second). Vertically 250 pixels correspond to 250 mm.

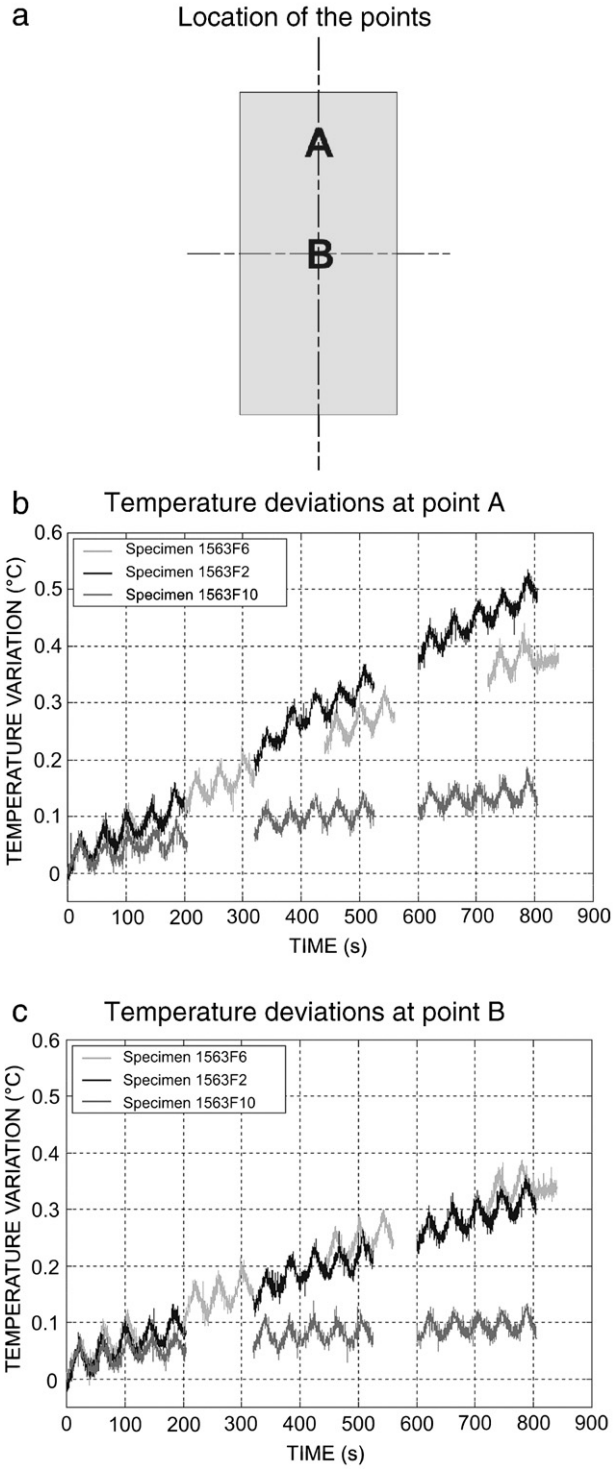

Fig. 9. Time variation of the temperature at two points of the specimens damaged by freezing–thawing cycles under cyclic quasi-static compressive loading.

occurs between the edges of the cracks. Thermal dissipations due to these frictional forces generate irreversible temperature increases in the sample. In this paper, we present two examples of thermal records for which significant thermal effects related to damage were observed. First, we present thermal observations of a mortar specimen during an up to failure compressive test. Then, we present thermal records of cyclic compressive tests performed on freeze–thaw damaged concrete samples.

3.3.1. Up to failure compressive test

Compressive tests were performed up to failure on a $40\times40\times160$ mm^3 mortar specimen. The material is described in Table 1. The controlled crosshead speed was fixed at 0.1 mm s^{-1}.

Fig. 6 shows the time variation of the compressive stress. Fig. 7 shows thermal maps of the surface at different times of the test. These pictures show an overall warming up of the specimen due to thermo-elastic coupling. On image 32, the first discernible localized thermal features appear and increase up to image 34. These first thermal effects correspond to the beginning of the softening domain (Fig. 6). At this moment, the compressive stress is about 40 MPa. From image 35 to image 39, the temperature variations homogenize. From image 40 onwards, temperature increases and localizes again up to the failure of the specimen.

It can be supposed that the first thermal effects (images 32–34) are due to the initiation of cracks which stabilized until image 39 before starting again up to failure (images 40 to 44). It must be mentioned that from image 40 to 44, scaling was observed on the surface of the specimen. This scaling implies a modification of the surface emissivity and does not permit quantitative interpretation of the thermal measurements to be done. The general warming of the specimen between images 40 and 43 can be attributed to thermal dissipation due to a distributed state of damage. Image 45 is taken after the failure when the load has dropped to zero while the crosshead displacement was proceeding. The overall temperature immediately decreased due to the stress release (thermo-elasticity) except in the failure zone due to friction between crack edges. Image 44 is probably taken immediately after the failure because the overall temperature started decreasing.

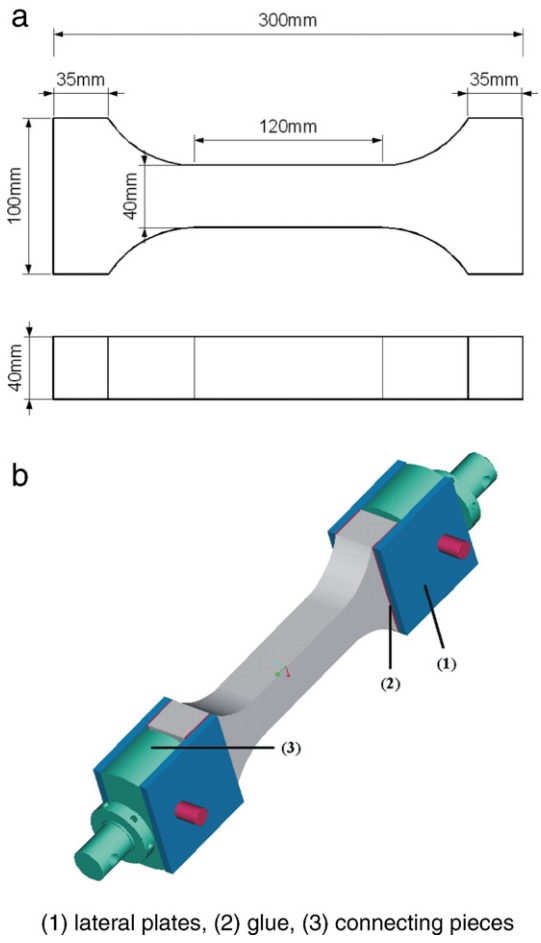

Fig. 10. a) Geometry of the specimens for direct tensile tests, b) Grip system.

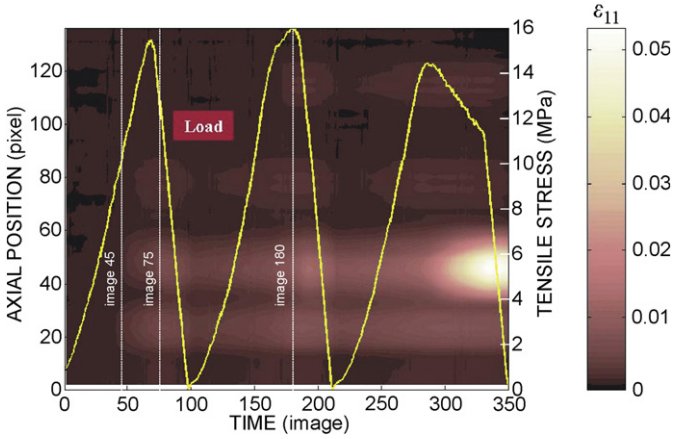

Fig. 11. Applied stress and time variation of the axial component of the strain tensor along the lengthwise axis in a specimen under cyclic quasi-static tensile loading. Vertically 120 pixels correspond to 100 mm.

3.3.2. Cyclic compressive tests on specimens damaged by freezing–thawing cycles

Cyclic compressive tests were performed on three concrete specimens (cross section 50×150 mm^2, length 300 mm) damaged by freezing–thawing cycles. The controlled crosshead speed was fixed at 0.05 mm s^{-1}. Fourteen freezing–thawing cycles were applied according to ASTM C666 with a cooling rate of 12 °C/h within the limits +5/−18 °C. The composition of the concrete is given in Table 1. The compressive strength was 40 MPa for non damaged concrete.

Fig. 8 shows the variation of the temperature profile along the lengthwise axis of the sample versus the image number for one specimen. For clarity reasons colour scale is different between Fig. 8-a, b, c and d. The overprinted curve represents the variation of the compressive stress. From the temperature scale, cyclic temperature variations can be observed in phase with the load, and can be attributed to the thermo-elastic effect. In addition, an overall warm-up can be noticed. Fig. 9 illustrates this phenomenon more clearly. It represents the time variation of the temperature at two points on the specimens. The overall warm-up reaches approximately 0.3 °C after 20 cycles for specimens 1563F6 and 1563F2. This warm-up is higher than the supposed drift of the thermal measurement system, which did not exceed 0.07 °C during the experiment. Hence, this temperature raise can be attributed to dissipative phenomena associated with damage in the concrete.

For specimen 1563F10, the temperature raise is lower than for the two other specimens. Although no particular investigation was performed to explain this difference, we can assume that differences in micro-structure (porosity, type of hydrates, orientation and location of micro-cracks, etc.) could have led to different damage consequences of the freezing–thawing cycles between 1563F10 and the other specimens.

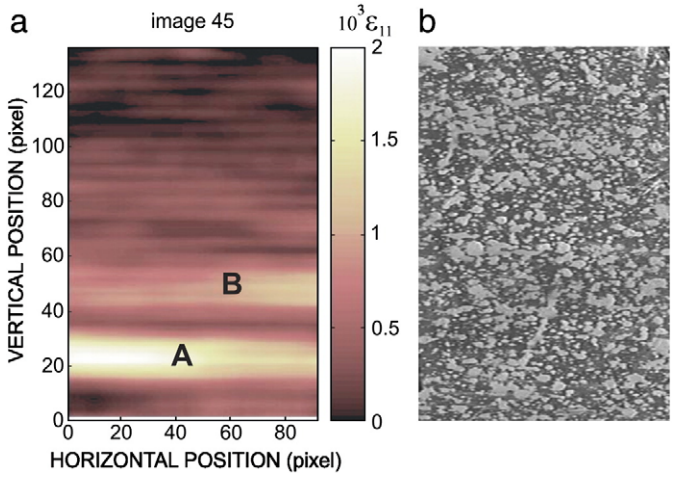

Fig. 12. Longitudinal strain field at image 45 and external aspect of the specimen at the same time. Vertically 120 pixels correspond to 100 mm, horizontally 90 pixels correspond to 40 mm.

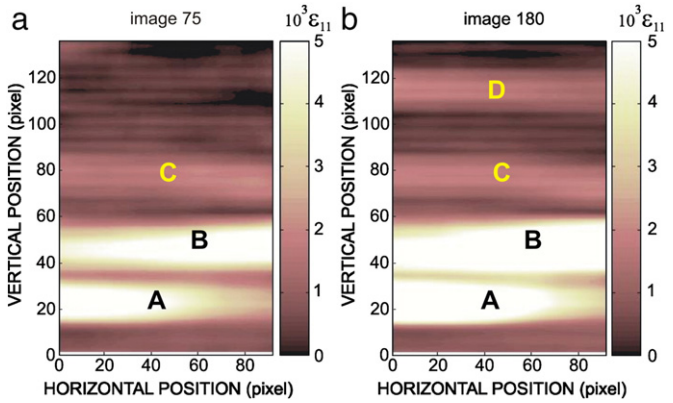

Fig. 13. Longitudinal strain field at images 75 and 180. Vertically 120 pixels correspond to 100 mm, horizontally 90 pixels correspond to 40 mm.

A theoretical approach based on virtual power principle and continuum damage mechanics was proposed in [18]. This model consists in an extension of an existing mechanical model of damage [19] to take account of thermo-elasticity and thermal effects of the damage. The modification mainly consisted in adding two terms in the expression of free energy. The first term allows the thermo-elastic effect to be modelled and leads to Eq. (1) previously presented. The second term introduces a coupling between temperature and a damage parameter β. This parameter links the elastic modulus of the undamaged material E_0 and the actual modulus E:

$$E = \beta \cdot E_0 \tag{3}$$

$\beta = 1$ for undamaged concrete and $\beta = 0$ for totally damaged material.

The thermal response of this model for a cyclic compressive loading simulation shows an overall warming superimposed with thermo-elastic temperature variations.

It confirms that the overall warming observed Fig. 9 can be attributed to the damage evolution in the material. Details about this theoretical approach which oversteps the scope of this article can be found in [18].

4. Strain field in a concrete specimen under tensile and flexural loads

4.1. Strain field measurement during a loading/unloading tensile test

Steel-fibre high-performance concrete specimens were subjected to loading/unloading tensile tests. The specimens are illustrated on Fig. 10. This figure also shows the mechanical system used to apply the tensile force to the sample. The controlled crosshead speed was fixed at 0.01 mm s^{-1}.

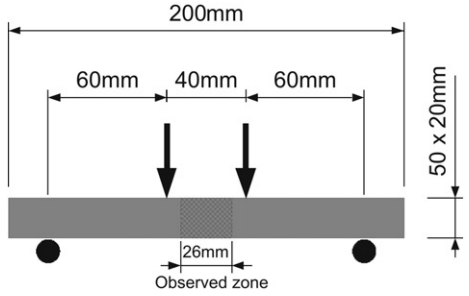

Fig. 14. Experimental setup for flexural experiments.

Strain field was determined using DIC. By means of a colour scale, Fig. 11 represents the time evolution along the lengthwise profile of the axial component of the strain tensor for a typical experiment. The overprinted curve is the time variation of the tensile stress. During this test, the maximum tensile stress reached 10 MPa. The tensile strength was 12 MPa in average. Figs. 12 and 13 show strain fields at various moments of the test. For clarity reasons colour scale is different between Figs. 11, 12 and 13.

Fig. 12-a, corresponding to image 45, shows two strain localization zones although the surface of the specimen looks intact (Fig. 12-b). Fig. 11 shows that image 45 corresponds to 67% of the maximum load. Localization phenomena already occurred despite the relative low loading level. By observing Fig. 12, the final fracture could be expected in zone A which is the most intense of both localization zones firstly appeared. At the beginning of the first unloading, a third localization zone, C, appeared as shown on Fig. 13-a, image 75. After the first unloading phase, one can observe in Fig. 11 that residual strains remain in localization areas A and B. In contrast, localization zone C – where strains were smaller than in A and B – vanishes. All the localization zones appear again at the beginning of the second loading cycle showing the irreversible nature of the localization phenomenon.

A fourth localization zone D appears at the second cycle peak (Figs. 11 and 13-b, image 180), showing the effect of the fibres in transmitting internal forces.

Lastly, during the third cycle, strains drastically increased in zone B where failure finally occurred.

4.2. Strain field measurement during a flexural test

Steel-fibre high-performance concrete beams were subjected to a 4-point bending load. The dimensions of the beam were $50\times50\times500$ mm^3. The experimental setup is described on Fig. 14. The crosshead speed was fixed at 5.10^{-2} mm s^{-1}. During the experiment, the strain fields of a 65 mm long central section of the beam were recorded using DIC. Fig. 15, which represents strain fields at various times, shows that three strain localization zones, marked A, B and C, appear early in the tensile zone of the beam. They can be suspected on image 30 and clearly appear on image 35, which corresponds to the end of the linear part of the load curve. Up to this point, the surface of the beam visually seemed undamaged. From image 50 onwards, most of the strains are concentrated within the localization zones. At image 70, a macro-crack occurred in the C localization zone. Notice that for clarity reasons colour scale changes between the different images of Fig. 15.

5. Conclusion

Some applications of infrared thermography and Digital Image Correlation to the analysis of the behaviour of concrete have been presented.

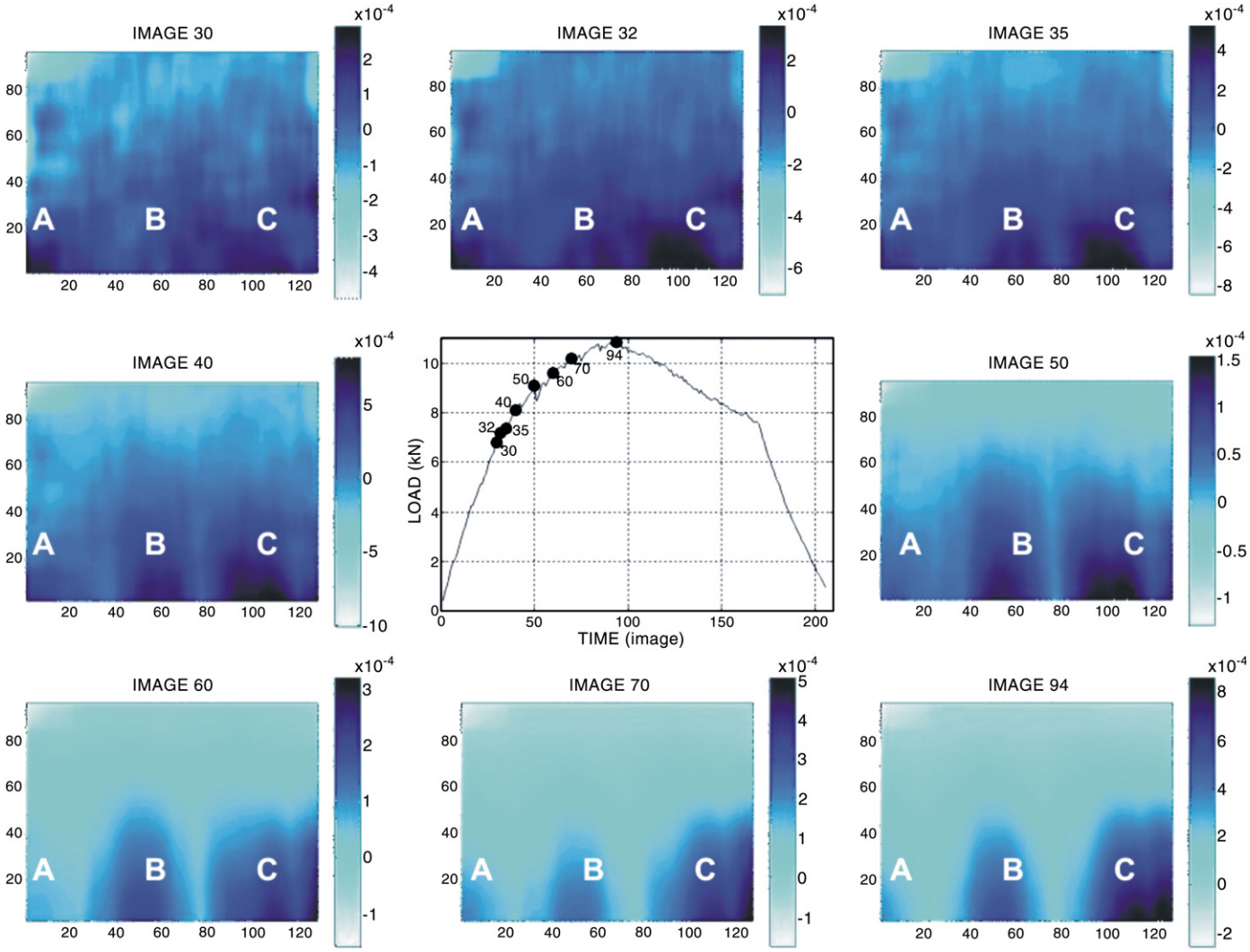

Fig. 15. Strain fields at various times during a 4-point flexural test performed on a SFHPC beam and time variation of the load. The dots on the curve localize the images.

Infrared thermography allowed us to accurately measure the thermo-elastic effect for mortar and steel-fibre high-performance concrete under compressive loads. During an up to failure test, infrared thermography showed localized thermal manifestations superimposed on the overall warming due to the thermo-elastic coupling. This localized effect related to damage was observed before the stress peak was reached and increased until failure occurred.

Thermal dissipation due to damage was also highlighted for plain concrete – damaged by freezing–thawing cycles – under cyclic loading: an overall warming due to damage superimposed on the cyclic temperature variations due to thermo-elastic coupling.

Digital Image Correlation (DIC) proved to be an efficient way to determine strain fields in a concrete specimen under load. In particular, this technique permits localization phenomena to be highlighted. Choi and Shah [5] previously investigated localization phenomena using DIC for concrete under compression. In this paper, localization effects are reported for specimens under tensile and flexural loadings. Early strain localization phenomena were detected indicating a heterogeneous damage state. The first strain localizations occurred before any damage was apparent on the surface of the specimens.

The complexity of the behaviour of concretes and the necessary improvement of the constitutive laws required by new design challenges justify the use of new and accurate methods of investigation. The image processing methods presented in this paper are likely to improve the knowledge of the behaviour of concretes. Numerous other aspects of their behaviour could be investigated by these methods: creep, shrinkage, concrete-steel bond, healing processes, chemical damage, etc. Moreover, increased interest rises from the coupling of both methods that allows simultaneous thermal and kinematic analysis to be done [20].

References

[1] M.P. Luong, Infrared thermovision of damage processes in concrete and rock, Engineering Fracture Mechanics 35 (1/2/3) (1990) 291–301.
[2] A. Chrysochoos, H. Louche, An infrared image processing to analyse the calorific effects accompanying strain localisation, International Journal of Engineering Science 38 (16) (2000) 1759–1788.
[3] T.C. Chu, W.F. Ranson, M.A. Sutton, W.H. Peters, Application of digital image correlation techniques to experimental mechanics, Experimental Mechanics 25 (3) (1985) 232–244.
[4] H.A. Bruck, S.R. Mc Neill, M.A. Sutton, W.H. Peters, Digital image correlation using Newton–Raphson method of partial differential correction, Experimental Mechanics 29 (3) (1989) 261–267.
[5] S. Choi, S.P. Shah, Measurement of deformations on concrete subjected to compression using image correlation, Experimental Mechanics 37 (3) (1997) 307–313.
[6] Y. Berthaud, S. Calloch, S. Collin, F. Hild, Y. Ricotti, Analysis of the degradation mechanisms in composite materials, through a correlation technique in white light, I.U.T.A.M. Symposium "Advanced Optical Methods and Application in Solid Mechanic, Poitiers University, France, 1998.
[7] B. Wattrisse, A. Chrysochoos, J.M. Muracciole, M. Némoz-Gaillard, Analysis of strain localization during tensile tests by Digital Image Correlation, Experimental Mechanics 41 (1) (2001) 29–39.
[8] B. Wattrisse, A. Chrysochoos, J.M. Muracciole, M. Némoz-Gaillard, Kinematic manifestations of localization phenomena in steels by image intercorrelation, European Journal of Mechanics A/Solids 20 (2001) 189–211.
[9] V. Huon, O. Maisonneuve, B. Wattrisse, J.M. Muracciole, Mise en évidence par granularité en lumière blanche de phénomènes de multilocalisation de la déformation pour les bétons de poudres réactives sollicités en traction, Comptes Rendus de l'Académie des Sciences – Series IIB – Mechanics 329 (2001) 897–900.
[10] V. Huon, B. Wattrisse, M.S. El Youssoufi, A. Chrysochoos, Elastic behavior of anisotropic terra cotta ceramics determined by kinematic full-field measurements, Journal of the Ceramic Society 27 (2007) 2303–2310.
[11] J.S. Lawler, D.T. Keane, S.P. Shah, Measuring three-dimensional damage in concrete under compression, ACI Materials Journal 98 (6) (2001) 465–475.
[12] D. Corr, M. Accardi, L. Graham-Brady c, S.P. Shah, Digital image correlation analysis of interfacial debonding properties and fracture behavior in concrete, Engineering Fracture Mechanics 74 (2007) 109–121.
[13] P. Richard, M. Cheyrezy, Les bétons de Poudres réactives, Annales de l'ITBTP Série béton 320 (352) (1995) 85–102.
[14] P. Richard, M. Cheyrezy, Composition of reactive powder concretes, Cement and Concrete Research 25 (7) (1995) 1501–1511.
[15] W. Thomson (Lord Kelvin), On the thermoelastic and thermomagnetic properties of matter, Transactions of the Royal Society, 20, 161, (1853) 57–77.
[16] BPEL91, Fascicule n°62, titre 1, section I du Cahier de Clauses Techniques Générales (CCTG).
[17] J. Lemaître, J.L. Chaboche, Mécanique des matériaux solides, Dunod, Paris, 1985.
[18] V. Huon, O. Maisonneuve, B. Cousin, Comportement thermomécanique d'un béton ordinaire en compression cyclée: expérience et modélisation, Comptes Rendus de l'Académie des Sciences – Série IIB – Mechanics 329 (2001) 889–896.
[19] M. Frémond, B. Nedjar, Damage, gradient of damage and principle of virtual power, International Journal of Solids and Structures 33 (8) (1996) 1083–1103.
[20] B. Wattrisse, J.-M. Muracciole, A. Chrysochoos, Thermomechanical effects accompanying the localized necking of semi-crystalline polymers, International Journal of Thermal Sciences 41 (5) (2002) 422–427.